

# Diffusion-wave laser radiometric diagnostic quality-control technologies for materials NDE/NDT

A. Mandelis\*

*Photothermal and Optoelectronic Diagnostics Laboratories (PODL), Department of Mechanical and Industrial Engineering, University of Toronto and Materials and Manufacturing Ontario, 5 King's College Road, Toronto, Ontario, Canada M5S 3G8*

## Abstract

The development of diffusion-wave diagnostic methodologies and their implementation as laser infrared photothermal radiometric diagnostics for industrial materials NDT, has resulted in two emerging NDE/NDT technologies. The solution of the ill-posed thermal-wave inverse problem has achieved reconstructions of thermal-diffusivity depth profiles in engineering materials such as heat-treated steels and thermal-barrier coatings. A novel approach for surface roughness elimination was introduced, modeling roughness as white (Gaussian) noise in the spatial coordinate. Furthermore, a novel semiconductor radiometric NDE metrology capable of measuring the primary photo-injected free carrier parameters (recombination lifetime, electronic and thermal-diffusivities, and surface recombination velocities) is also being developed. These emerging diffusion-wave technologies are described, and examples/case studies involving manufactured and thermally processed steels, thermal-barrier coatings and industrial Si wafers are discussed. © 2001 Elsevier Science Ltd. All rights reserved.

*Keywords:* Diffusion-wave technologies; Laser radiometric diagnostics; NDE/NDT; Metals; Semiconductors; Depth-profilometry

## 1. Introduction/background

Among the modern-day nondestructive testing (NDT) methodologies, thermal-wave detection is a diffusion-wave technique [1,2] growing in importance due to its ability to monitor subsurface structures and damage in materials, well beyond the optical penetration depth of illumination sources, i.e. below the range of optical imaging for opaque materials. Mathematically, diffusion-wave fields are oscillatory harmonic solutions to diffusion-equation boundary-value problems. Their major common feature is a complex wave vector, which leads to spatially heavily damped pseudo-propagation, and a frequency-dependent ‘skin-depth’ called the diffusion length. Most familiar to the NDT community is the ac Eddy current technique [3], and thermal-waves [4]. Photothermal techniques involve launching a thermal-wave in a sample through laser excitation and detection of the resulting temperature at an external boundary of the sample. The most common photothermal signal generation methods include single-frequency harmonic excitation using a sinusoidally modulated continuous wave (CW) laser source and lock-in detection of the frequency-dependent temperature, or pulsed excitation and observation of the transient signal. The major advantage of

the former method is its superior signal-to-noise ratio (SNR) and the high damage threshold of relatively poor thermal conductors. Here the penetration (or diffusion) depth,  $\mu$ , is governed by the thermal-diffusivity,  $\alpha$ , of the medium, and the angular modulation frequency,  $\omega$ , of the laser beam intensity:  $\mu(\omega) = (2\alpha/\omega)^{1/2}$ . The amplitude and phase of the thermal-wave in inhomogeneous materials carry information about any heat transport disruption or change below the surface. In view of the ill-posed nature of the diffusion-wave inverse problem [5], great care must be taken in generating appropriate mathematical models for inverting these signal channels in order to yield reliable depth reconstructions of the spatially variant thermal-diffusivity of the sample. In recent years several attempts and breakthroughs have been made in inverting these data and thus reconstructing arbitrary thermal-diffusivity (or conductivity) depth profiles [6–10]. These have been summarized by Mandelis et al. [9]. By far, the most popular experimental methodology used with this thermal-wave inverse problem has been laser infrared (IR) photothermal radiometry (PTR) owing to the completely remote and non-intrusive nature of this technique [7,11]. A schematic diagram of the experimental apparatus is shown in Fig. 1. An Ar-ion laser (514 nm) modulated by an acousto-optic modulator is directed onto the sample surface. The beam is broadened with a diffuser to attain a larger spotsize for one-dimensional (1D) analysis. A lens can be placed after the diffuser to achieve a sharp focus

\* Tel.: +1-416-978-5106; fax: +1-416-266-7867.

*E-mail address:* mandelis@mie.utoronto.ca (A. Mandelis).

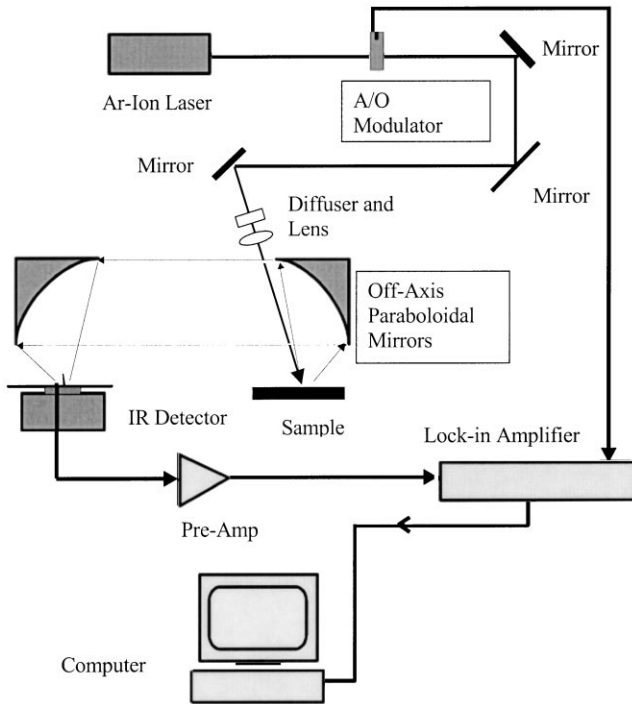


Fig. 1. Schematic diagram of typical laser photothermal infrared radiometric set-up for thermal-wave and electronic carrier plasma-wave NDT.

with spot-size of approximately  $25 \mu\text{m}$ , if so required. The emitted IR radiation from the sample surface is collected and focused onto the detector using two off-axis paraboloidal mirrors. The detector is a liquid  $\text{N}_2$  cooled  $\text{HgCdTe}$  element with an active area of  $1 \text{ mm}^2$  and a spectrally selective range of  $2\text{--}12 \mu\text{m}$ . A germanium window with a transmission bandwidth of  $2\text{--}14 \mu\text{m}$  is mounted in front of the detector to block any visible radiation from the pump laser. The detector signal is preamplified before being sent into the lock-in amplifier. The two lock-in amplifier outputs, amplitude and phase, are recorded across a range of laser modulation frequencies.

In the first part of this paper, the state-of-the-art in depth profilometric PTR as an emerging NDT technology for engineering materials inspection and process quality-control will be presented and some case studies will be discussed as examples of the inverse-problem-based depth profilometric capabilities of the technique. The second part of this paper deals with another radiometric diffusion-wave technique based on an additional PTR signal source, which usually dominates electronic materials [12,13]. Following super-bandgap optical excitation, the harmonically generated PTR signal consists of two contributions: one from the de-exciting and diffusing modulated carrier density (a diffusion-wave called the ‘plasma-wave’), and another from direct absorption and non-radiative energy conversion (heating) of the lattice (‘thermal-wave’). The plasma-wave component is generated by direct IR emission from photo-excited carriers (electrons or holes), each free carrier acting as an individual Planck radiator. Therefore, the signal

carries information about the density of photo-generated free carriers and their subsequent recombination kinetics, a measure of the electronic trap densities and of the electronic quality of the semiconductor material. The development of an industrially viable PTR technology at the University of Toronto for semiconductor metrology is discussed, including several case studies.

## 2. Thermal-wave depth profilometry

### 2.1. Thermal-diffusivity reconstructions in processed metals

Thermal-diffusivity which depends on the microstructural properties of a material, is very sensitive to the changes that take place in the material as a result of surface modification processes, such as laser processing, case hardening and coating deposition. Considering this change in thermal-diffusivity and the typical depths involved (a few micrometers to a couple of millimeters), photothermal techniques have proven to be a good non-destructive and non-contact method of profiling these subsurface inhomogeneities [7–11]. In the development of PTR as a depth profilometric NDT technology, the inversion methodology based on the generalized theoretical formulation [9] was applied to manufactured steel-based materials. A detailed description of the analytical/computational procedure can be found elsewhere [14]. In practice, the pump beam spot size is made much larger than the maximum profiling depth,  $\mu(\omega_{min})$ , using the optical diffuser to maintain the 1D thermal-wave formalism assumed in the theory. An exponential thermal-diffusivity profile of the form

$$\alpha_s(x) = \alpha_0 \left( \frac{1 + \Delta e^{-qx}}{1 + \Delta} \right)^2; \quad \Delta = \frac{1 - \sqrt{\alpha_L/\alpha_0}}{\sqrt{\alpha_L/\alpha_0} - e^{-qL}} \quad (1)$$

is assumed, where  $\alpha_0$ ,  $\alpha_L$ ,  $q$  are constants representing the values of the thermal-diffusivity at the two boundary surfaces ( $x = 0, L$ ) of the material, and the diffusivity gradient, respectively. The radiometric signal in the back-scattering mode is given by [15]

$$S_B(\omega) = K(\omega)\Delta T(0, \omega), \quad (2)$$

where  $K$  is an instrumental constant depending on geometrical factors, the surface emissivity averaged over the spectral bandwidth of the detector, and on the Stefan–Boltzmann constant. The expression for the surface temperature  $\Delta T(0, \omega)$  was derived in [9]. In practice, the surface temperature response to the incident optical beam on the sample is normalized by the surface temperature response to the same beam at the same frequency of a semi-infinite homogeneous material (reference). This gives for each frequency a data-pair, namely amplitude ratio and phase difference between sample and reference. The normalizing procedure is necessary for the correct accounting of all frequency dependencies in the apparatus other than that due to the investigated sample. Theoretical

values are calculated from the data-pairs in the complex form  $|M(\omega)| e^{i\Delta\phi(\omega)}$  = complex PTR signal [9], where  $|M(\omega)|$  is the experimental amplitude ratio and  $\Delta\phi(\omega)$  is the phase difference at angular frequency  $\omega$ . Assuring the one-dimensionality of the problem by monitoring phase saturation as a function of laser beam size is extremely important for the reliability of diffusivity depth profile reconstructions. The values of amplitude, phase and the derivative of the phase are compared with the experimental values in calculating the local parameters  $\alpha_0$ ,  $\alpha_L$ ,  $q$  at each frequency using a customized two-dimensional Broyden method [9,16]. In reconstructing depth profiles from data it is very important to first find a reliable set of initial values for  $\alpha_0$ ,  $\alpha_L$ , and  $q$ . This can be achieved by finding the best fit to the first two-to-three points (high-frequency end) to the theoretical values calculated from  $|M(\omega)| e^{i\Delta\phi(\omega)}$  = complex PTR signal [9], assuming a single profile of the form given by Eq.(1).

In one set of experiments, two hardened samples made of C15 steel were investigated. The surface hardening of these samples was achieved by dissolving additional carbon through the surface (carburization) and subsequent thermal treatment. The thickness of the hardened layer was varied by changing the carburization time from sample to sample. The two samples investigated here had different carburization times. The steel samples could be treated as layers of thickness  $L$  (in this case 2 mm) on a homogeneous substrate (air). It was necessary to use a finite thickness layer theory for depth reconstruction in order to obtain reliable profiles for these samples [17]. The resulting diffusivity profiles together with the available microhardness profiles are shown in Fig. 2A. Although the diffusivity profiles do *not* show an identical inverse relation to the hardness profiles, the variations from sample to sample are well correlated. To confirm the validity of the finite thickness reconstruction methodology the sample no. 2 was machined down to a thickness of 1 mm from the side opposite to the profile shown in Fig. 2A. Then data were collected again from the case-hardened side and also from the machined side. The reconstructed profiles are shown in Fig. 2B. A portion of the profile obtained from the data taken from the hardened side is also shown in Fig. 2A to compare with the profile reconstructed when that sample was 2 mm thick. The difference between those two profiles in Fig. 2B is the accuracy tolerance of the current state-of-the-art PTR thermal-wave reconstruction methodology.

Fig. 3 shows a profile reconstructed from the data obtained from both sides of a case-hardened steel sample of thickness 1.75 mm. Here the substrate is air. It was not possible to reconstruct data beyond a depth of about 1 mm due to the three-dimensional (3D) effects associated with lateral thermal transport at very low modulation frequencies. A hardness profile obtained from one side of the sample was also used for comparison and exhibited very good anti-correlation with the diffusivity profile of Fig. 3.

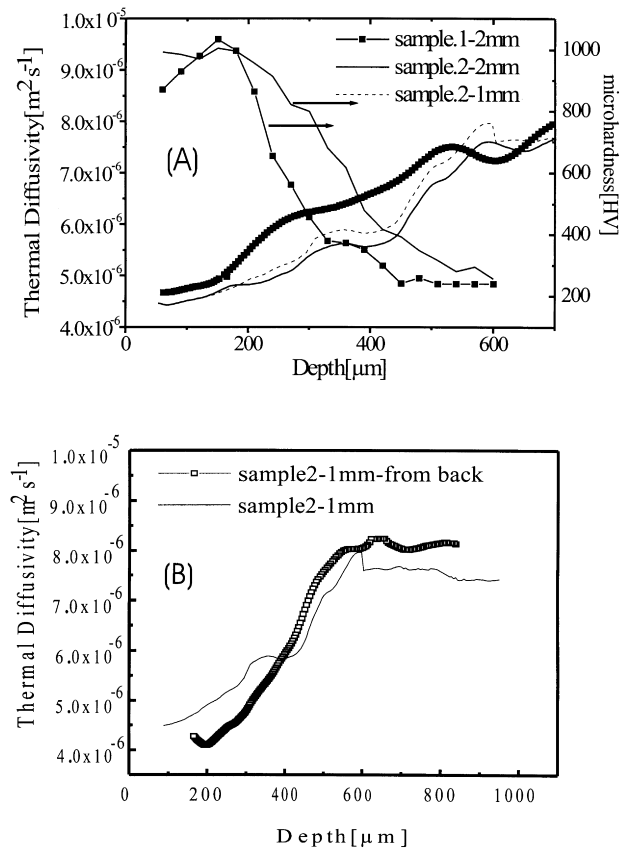


Fig. 2. (A) Reconstructed thermal-diffusivity depth profiles from PTR data and the corresponding microhardness profiles for the case-hardened steel samples: sample 1 ( $\square$ ) and sample 2 ( $\circ$ ); also shown is the profile after machining sample No. 2 to 1 mm thickness (---). (B) Reconstructed profiles from the two sides of the 1 mm sample.

## 2.2. Thermal-diffusivity reconstructions in rough thermal-sprayed coatings

Carbon steel substrates with various thermal spray-coatings (tungsten carbide, aluminum, and 316 stainless steel) were examined. A 1D thermal-wave model of a rough coating as a discrete homogeneous overlayer on a (homogeneous) carbon steel was generated and compared with PTR experimental results [18]. Thermal-sprayed coatings of tungsten carbide (WC17 Co), 316 stainless steel and aluminum were applied to 9.5 mm thick, 1018 steel rectangular bars. The tungsten carbide and stainless steel coatings were applied using the high velocity oxy-fuel (HVOF) process with the JP-5000 spray system. The aluminum coatings were applied with the electric arc method. The substrate was solvent cleaned after saw-cutting to remove cutting oils, then grit-blasted with 36 grit  $Al_2O_3$  at 758.6 kPa (110 psi) for approximately 1–2 min and followed by solvent wipe. The substrate panels were then sprayed to produce a controlled nominal thickness. For each coating type, all four-thickness panels were placed in the fixture together as a set, in order to lessen the variability between panels. The various nominal thicknesses (70–800  $\mu\text{m}$ ) for

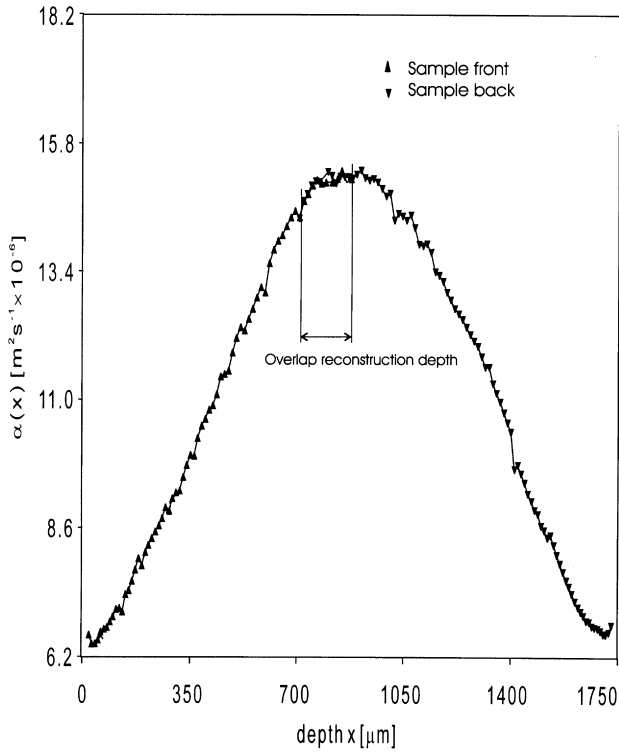


Fig. 3. Reconstructed thermal-diffusivity profiles from both sides of a case-hardened steel sample of 1.75 mm thickness.

each coating are reported in Table 1. Another set of samples that had two sizes of brass inserts (3.2 and 9.5 mm) and a nominal thickness of spray-coating (305 μm) was used for interface adhesion examination. The inserts were ground down to be flush with the face of the carbon steel panel with a light grit flapper wheel and then spray-coated. The thickness of the roughness-equivalent-layer ( $L_1$ ) was measured by a surfometer and is the value that gave the best fit. The  $R_t$  (peak-to-peak) value of the roughness was recorded. SEM pictures of the three coating samples were also obtained.

For the low frequency range scans (1–1000 Hz) a defocused beam (~6 mm diameter after the diffuser) was used to minimize 3D effects of heat diffusion. A bare laser beam (~1 mm diameter) was used for the higher frequency range (1–100 kHz). All measured PTR signals from the thermal-sprayed coatings were normalized to a Zr alloy

reference sample in order to account for the instrumental frequency dependence.

The amplitude (a) and phase (b) of typical normalized PTR signals for tungsten carbide (WC17 Co), stainless steel (316 SS) and aluminum samples are shown in Fig. 4. Two maxima and one minimum are observed for WC17 Co and 316 SS measurements. This signal frequency-response is due to thermal-wave interference resulting from coherent energy confinement within the spray-coating layer. The minimum of the phase signal shifted to higher frequencies as the coating thickness decreased. At higher frequencies the surface effects become more dominant and the observed spectrum may exhibit a strong contribution for roughness effects. The PTR signals from the stainless steel coating showed similar interference structure as in tungsten carbide. The minimum in the phase is also shifted to the right as the thickness of the coating decreases. The square root of the inverse of the frequency corresponding to this phase minimum vs. coating thickness is shown in Fig. 5a and b. A linear relation was found for the WC17 Co and 316 SS. This suggests that the PTR method can be used for thickness determination of these types of thermal spray-coatings once proper calibration is done. The PTR signal frequency-response of aluminum coatings differed significantly from the other coatings (WC17 Co and 316 SS). The difference can be attributed to the visibly larger roughness and porosity profile present on the surface of the aluminum coatings.

By comparing the experimental PTR measurements to the theoretical curves obtained from the 1D 3-layer photo-thermal model [18], the thermophysical parameters (thermal conductivity and diffusivity) of the thermal-sprayed coatings can be determined. A multi-parameter algorithm that minimizes the square of the difference between the calculated and the experimental amplitude and phase of the PTR signal was used to determine these parameters. The results are shown in Table 1.

In the frequency-domain roughness is observed across the entire scanned frequency spectrum. The foregoing multi-layer theoretical model, however, was found to be too simplistic in that it represents roughness as a discrete constant-property layer on top of a homogeneous coating and a semi-infinite substrate. With low-level roughness the results are satisfactory. As the level (thickness) of roughness increases, the thermal-wave spectrum becomes more complicated, especially at high frequencies, affecting to a

Table 1  
Thermal-diffusivity and conductivity values determined from the 3-layer and Gaussian methods for (a) tungsten carbide (WC17 Co), (b) stainless steel 316 (SS) and (c) aluminum [18]

Sample	Thickness $L_2$ (μm)	Multilayer method		Gaussian method		Roughness $L_1$ (μm)
		$K_2$ (W/m K)	$\alpha_2$ (m <sup>2</sup> /s) × 10 <sup>-6</sup>	$K_2$ (W/m K)	$\alpha_2$ (m <sup>2</sup> /s) × 10 <sup>-6</sup>	
Tungsten carbide	73.7–373.4	8.9–15.0	3.5–4.5	9.7–16.1	3.5–4.7	15–19
Stainless steel 316	160.2–718.8	8.1–9.0	1.5–2.6	5.8–9.6	1.6–2.3	51.7–68.0
Aluminum	152.0–802.0	21.0–45.0	33–55	–	–	111.0–120.0

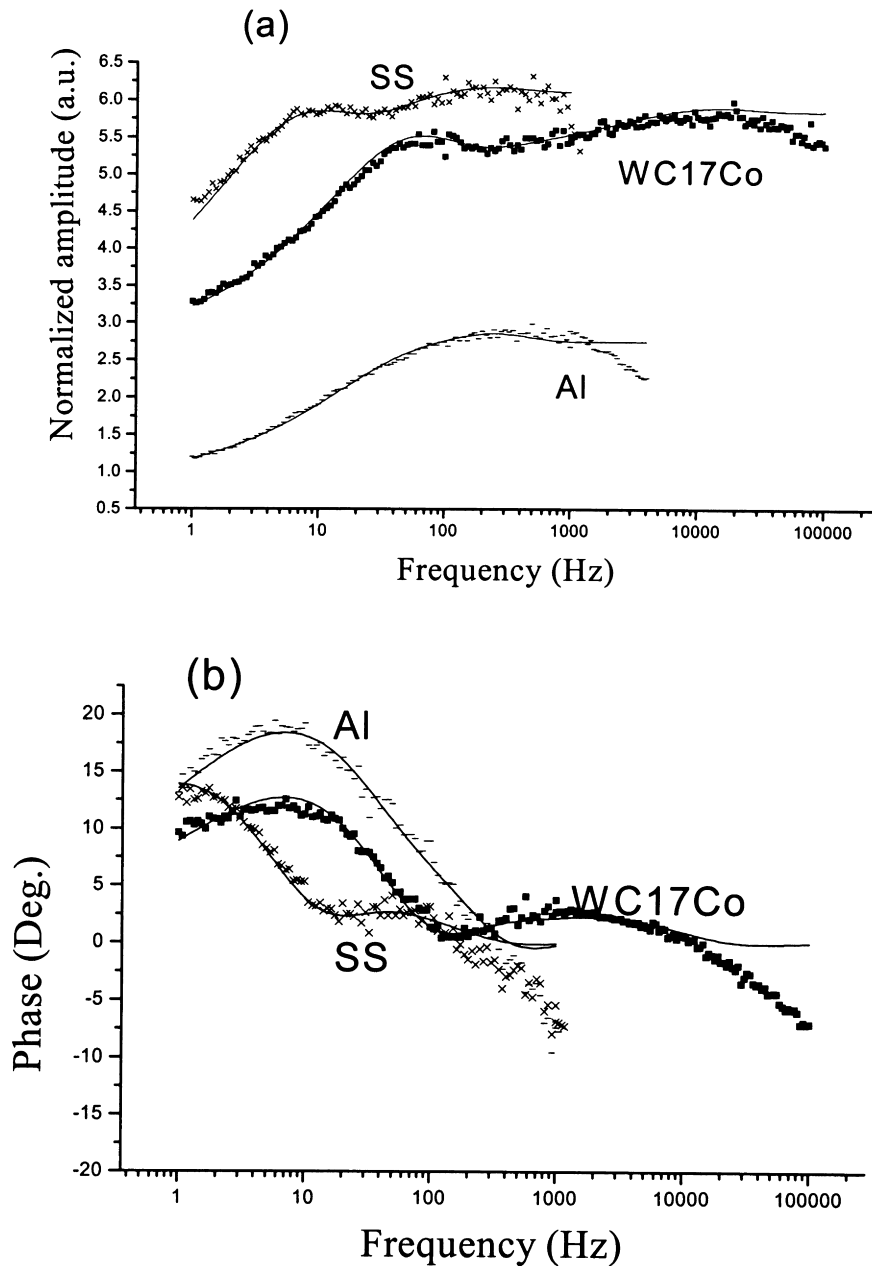


Fig. 4. Typical best-fit curve (solid lines) and experimental PTR signal for carbon steel samples with a tungsten carbide (solid squares), stainless steel (x-x-x) and aluminum (bars) thermal spray-coatings. (a) Amplitude. (b) Phase.

greater extent, the thermal-diffusivity and conductivity values obtained by this method. Using the concept that random roughness is equivalent to white (Gaussian) noise in the spatial depth coordinate, a more refined model can be obtained. Through a spatial Fourier transformation it is expected that the roughness spatial Gaussian profile will be mapped also as a Gaussian distribution in the frequency coordinate. This distribution is theoretically centered on a characteristic roughness length/depth. By extension, there can be a linear superposition of several such Gaussians, if there are multiple characteristic roughness scales associated with a particular surface. The Gaussian roughness

elimination method is based on recognizing distinct features (phase maxima) in the frequency spectrum. Since roughness is associated with the surface of a sample the effects are strongest at high frequencies, whereas the low frequency end is mostly related to substrate inhomogeneities. The objective of the method is to deconvolute the roughness spectrum from the underlayer thermophysical property depth profile (homogeneous or inhomogeneous). Therefore, in order to retrieve and eliminate roughness from the experimental curves a Gaussian fit to the high-frequency end is made, based on the theoretically expected Gaussian-to-Gaussian spatial Fourier transformation. Using the obtained

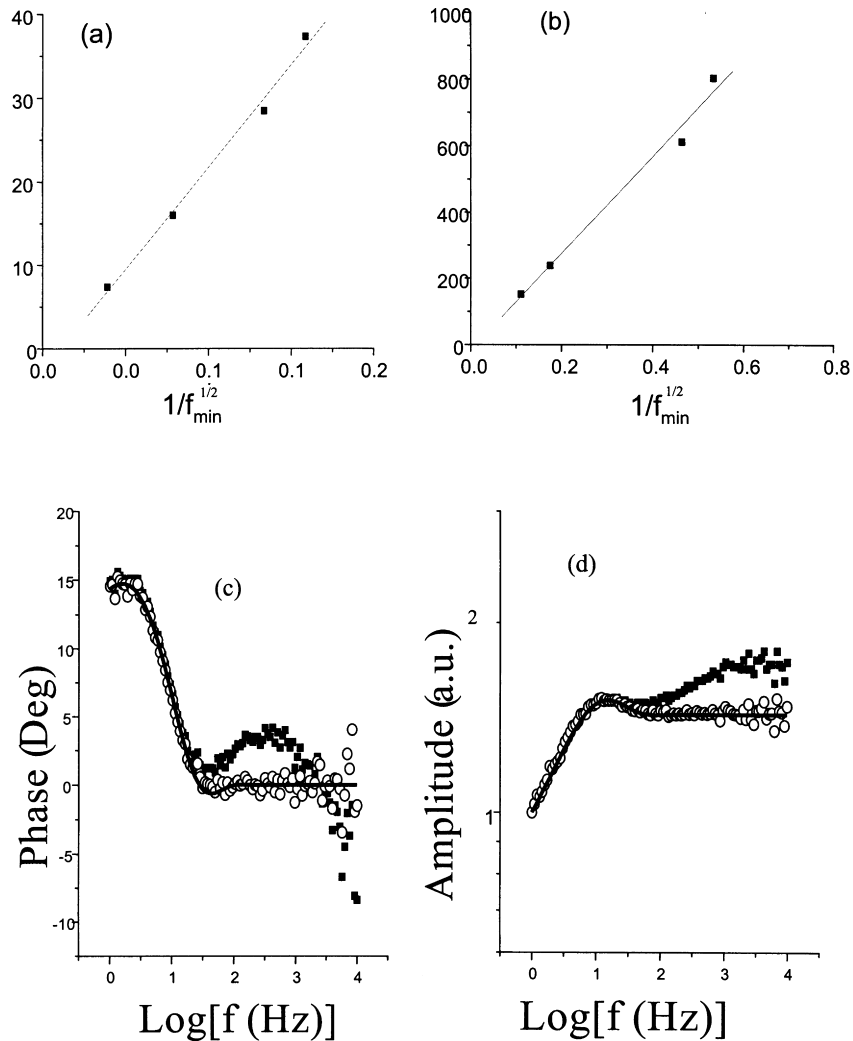


Fig. 5. Thermal spray-coating thickness vs. the inverse of the square root of the frequency corresponding to the phase minimum, see Fig. 4. (a) Tungsten carbide (WC17 Co); (b) stainless steel thermal spray-coatings; (c) PTR phase; and (d) amplitude frequency-response from a stainless steel thermal spray-coating on carbon steel substrate. The solid symbols represent the original PTR data with roughness effects at high frequencies. The open circles represent the experimental data after the application of the roughness elimination procedure. The solid line is the best fit using a 1D theoretical model [18] to corrected experimental data.

Gaussian fit, the experimental curves are corrected for roughness, thus revealing the contribution to the signal of the underlying coating. These corrected curves are then fitted to the 1D multilayer model (coating on semi-infinite substrate only), thus determining the thermophysical properties of the coating. In order to compare the equivalent-layer and spatial Gaussian profile methods for roughness elimination, the thermophysical properties of the tungsten carbide and stainless steel samples were obtained for the Gaussian profile, Table 1. The amplitude (c) and phase (d) of the normalized PTR signal of a stainless steel sample are shown in Fig. 5c and d. The Gaussian method was applied to this sample, and the roughness-corrected experimental data were subsequently fitted to a 1D model of one layer on a semi-infinite substrate. It was found that the values of the thermophysical properties obtained by the Gaussian-fit method do not change drastically from those

obtained from the multilayer method for these particular samples. However, the main advantage of the Gaussian method over the multilayer method, is that there is no need to introduce thermophysical variables for the rough layer, which may compromise the uniqueness of the solution obtained by the multi-parameter fitting procedure. The aluminum frequency-response could not be fitted with a single-Gaussian distribution satisfactorily due to the great extent of the rough layer. Multi-Gaussian fits are under way for this coating and will be reported in a future publication.

For comparison purposes the thermal conductivity and diffusivity of tungsten carbide at 1000 K, stainless steel 316, and aluminum are reported in Table 2. Our PTR-measured thermophysical values are consistent with the ones reported in the literature. Since the thermal-sprayed coatings have higher porosity than the metallic samples,

Table 2  
Literature values of thermal properties for WC, SS and Al

Material	Reference	$K$ (W/m K)	$\alpha$ (m <sup>2</sup> /s) $\times 10^{-6}$
316 Stainless steel	[22,23]	13.8	3.7
WC (1000 K)	[19–21]	40	10.2 <sup>a</sup>
Aluminum	[22,23]	237	98
Carbon steel 1018	[23]	51.9	16.5

<sup>a</sup> Diffusivity calculated from  $\alpha = k/\rho C_p$ .

the conductivity and diffusivity are expected to have lower values, as the measurements show.

### 3. PTR of electronic materials (semiconductors)

The measurements of photo-excited excess carrier lifetime and activation energies in a semiconductor are useful in the NDT and characterization of the electronic quality of semiconductor materials and in evaluating the performance of working semiconductor devices. The non-contact method of frequency-domain PTR detection has been shown to be promising for remote on-line or off-line impurity/electronic defect diagnostics [12]. In this section we report results of several case studies in the emerging technology of PTR of electronic materials. According to a statement of Kirchhoff's Law of detailed balance, reflecting conservation of energy, *at thermodynamic equilibrium the rate of emission of blackbody radiation from the surface and throughout the bulk of a material can be measured from, and is exactly equal to, the rate of absorption of the radiation incident on the material per wavelength interval.* Therefore, the IR emission spectrum for a de-excitation process in a semiconductor can be obtained directly from its (usually better known) absorption spectrum. In PTR detection, it is rather the reverse application of Kirchhoff's Law that is exploited: optical absorption of a laser beam in the ultraviolet, visible or near-IR (super-bandgap) spectral range in Si, for example, results in electronic excitation, followed by complex ultrafast intraband decay processes, and ultimately by much slower interband recombination kinetics. A fraction of the de-exciting electronic cloud recombines upon emission of IR (blackbody) radiation, *which is equivalent to surface and bulk absorption of the same IR flux integrated over the same depth coordinate*, in agreement with Kirchhoff's Law. The excess energy due to carrier thermalization and any direct lattice absorption and optical-to-thermal energy conversion, are also detected as an additional increase in blackbody emission, in agreement with the linearized Eq. (2). In practice, this contribution to the PTR signal in industrial-quality Si wafers occurs at very low frequencies (<1 kHz). Therefore, signal analysis can be done entirely within the framework of free carrier diffusion and recombination under harmonic excitation conditions (a plasma-wave) [13] at higher frequencies.

#### 3.1. PTR of SiO<sub>2</sub>/Si MOS capacitors

The theoretical analysis of the dominant electronic component of the PTR signal from a p-type semiconductor material/wafer of thickness  $L$ , under high-absorption conditions (514 nm) gives [19]

$$\Delta Q = \frac{N_0}{\sigma_n^2 D_n + \sigma_n s_1} C(\lambda_1, \lambda_2) \left[ \frac{(1 - e^{-\sigma_n L})^2}{1 + \Gamma_1 e^{-2\sigma_n L}} \right] \quad (3)$$

where  $N_0$  is the number of photo-injected n-type carriers at the surface,  $s_1$  the front surface recombination velocity and the complex plasma-wave vector  $\sigma_n$  is defined as:

$$\sigma_n = \sqrt{\frac{1 + i\omega\tau}{D_n\tau}} \quad (4)$$

$D_n$  is the ambipolar carrier diffusion coefficient and  $\tau$  is the recombination lifetime.  $C$  is an instrumental constant.  $\lambda_1(\lambda_2)$  is the lower (upper) limit of the detection bandwidth of the IR detector  $\Gamma_1 = (D_n\sigma_n - s_1)/(D_n\sigma_n + s_1)$ .

In one particular case study, off-line quality-control analysis of SiO<sub>2</sub>/Si interfaces of full-size Si wafers with metal-oxide-semiconductor (MOS) capacitor structures has been performed using PTR. A fitting procedure which uses the amplitude and phase frequency-responses has been developed and has been shown to be quite sensitive to changes in carrier diffusivity ( $D_n$ ), carrier lifetime ( $\tau$ ) and surface recombination velocity ( $s$ ) [19]. Fig. 6 shows the PTR lifetime temperature dependence of two samples W1 (Al-gated MOS structure) and W2 (polysilicon-gated MOS structure), obtained by fitting the data to Eq. (3). The increase in  $\tau$  with temperature observed for both wafers follows the Shockley–Reed–Hall theory [20,21], which assumes that the thermally increased density of intrinsic carriers fills up existing trapping sites and thus increases the photo-injected carrier lifetime. The corresponding Arrhenius plots of the PTR lifetimes and the calculated activation energies are presented in Fig. 7. The activation energy value of  $\Delta E = 0.21$  eV obtained for sample W2 is probably due to the near-interface shallow electron trap produced during the gate layer growth. The lifetime information obtained, Fig. 7, shows that the poly-Si gate MOS devices are predicted to exhibit better performance than the metal-gated ones, as expected from the relative unavailability of metallic deep levels in the former capacitors, which are known to act as lifetime killers.

#### 3.2. Microelectronic circuit characterization via PTR measurements of scribeline recombination lifetimes

The samples used in this case study were four 4 in. wafers of p-type Si, with patterned device structures. The wafers had been oxidized with a 1000 Å gate oxide. Polycrystalline Si (polysilicon) was deposited and patterned to form pads of different sizes and shapes. Fig. 8a shows an optical microscope photograph of two different sizes of scribelines. One

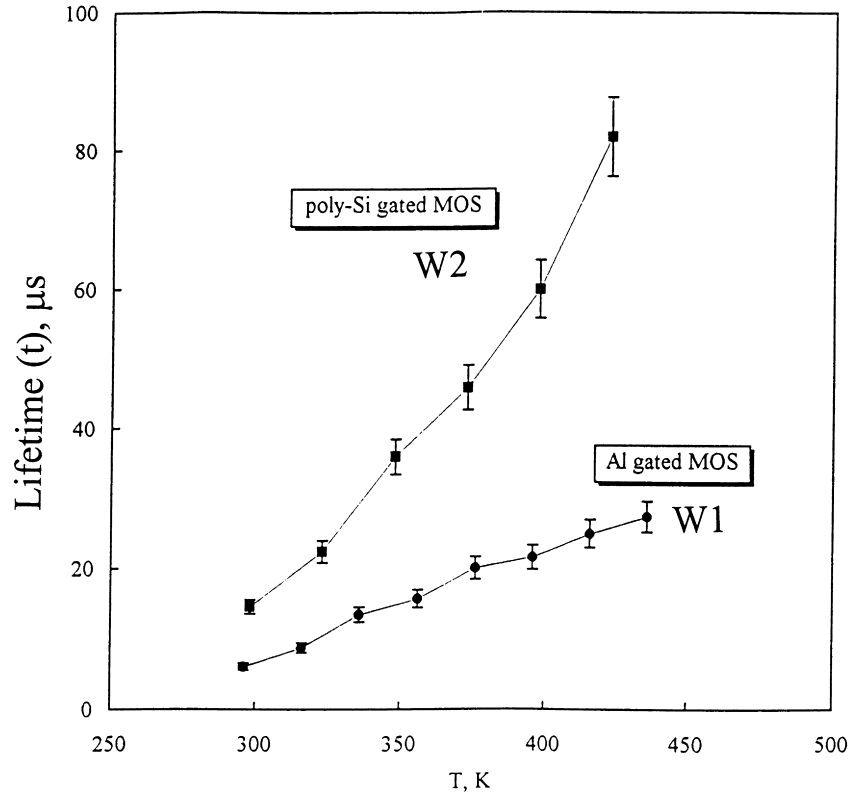


Fig. 6. PTR lifetime temperature dependencies of sample W1 (●) and W2 (■).

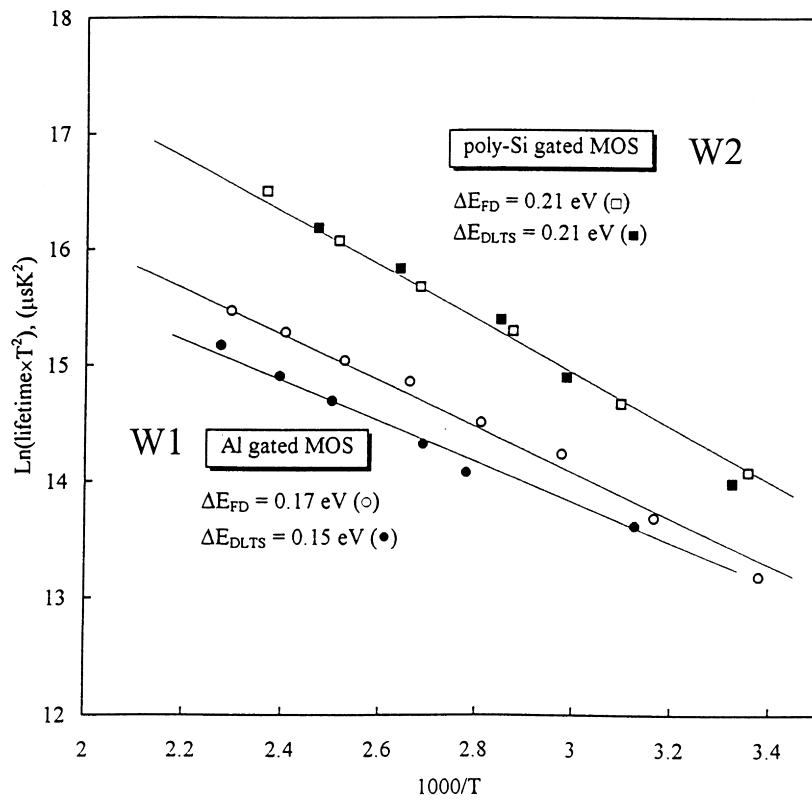


Fig. 7. Arrhenius plots of the PTR-measured lifetimes in Fig. 6. The deep-level transient spectroscopy values were measured using PTR [24].

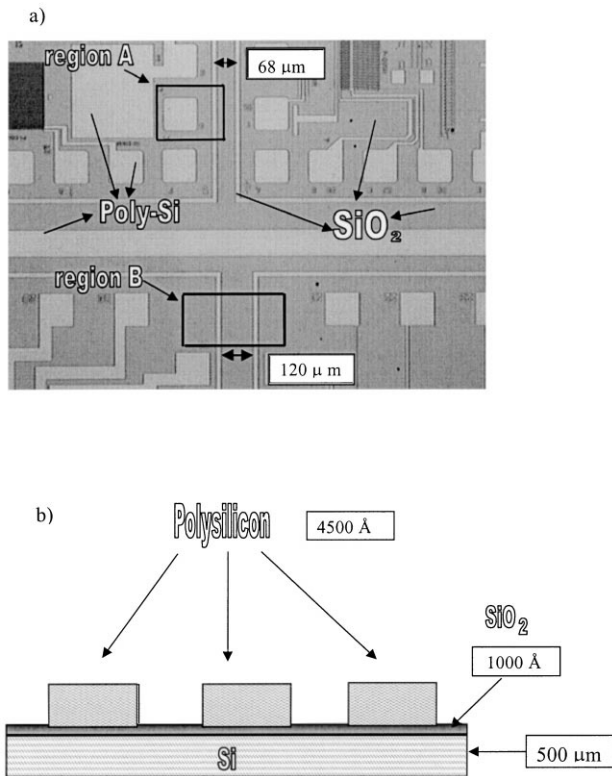


Fig. 8. (a) Microscope photograph showing two different sizes of scribe-lines in a patterned wafer. (b) Schematic representation of the cross-sectional geometry of the wafers.

type of scribeline was  $120\ \mu\text{m}$  in width; the other type was about  $68\ \mu\text{m}$  wide. Bright structures are light scattering poly-Si pads or devices, whereas darker regions are the more highly reflecting  $\text{SiO}_2$ -Si interfaces. Fig. 8b is a schematic of the cross-sectional geometry of the wafer. The poly-Si thickness was about  $4500\ \text{\AA}$ .

The experimental set-up used for the PTR frequency scan probing and imaging inside and outside the scribelines is essentially that of Fig. 1. Radiometric images were generated using a manual scanning system. These images are PTR amplitude and phase scans at a fixed laser-beam-intensity modulation frequency. In recent work it has been shown that the amplitude scales linearly with the recombination lifetime in some ranges of parameters [22]. Therefore, an ( $x$ - $y$ ) amplitude scan of Si substrate (with or without the presence of oxide) when it is properly calibrated in units of  $\mu\text{s}$ , yields, in principle, a recombination lifetime image of the scanned region. Such a radiometric image has been called a 'thermoelectronic image', or a 'thermoelectronic scan'. The resolution of each spot was  $20\ \mu\text{m}$ . Beam size was estimated to be  $48\ \mu\text{m}$  using a charge-coupled-device (CCD) camera and optical scan measurements through a  $5\ \mu\text{m}$  pinhole. The laser power was about  $40\ \text{mW}$ , which corresponds to a low injection level. On scanning across typical wafer structures shown in Fig. 8, the CCD camera was used to determine the desired location and to guide the laser beam inside or around the neighborhood of a given scribeline.

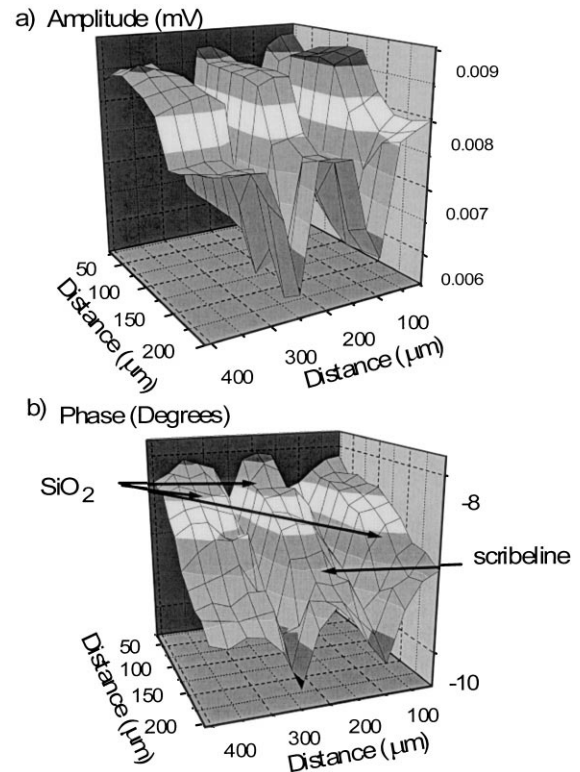


Fig. 9. (a) PTR signal amplitude and (b) phase; thermoelectronic images for region B shown in Fig. 8a.

A scribeline junction ( $120\ \mu\text{m}$  width), approximately  $2\ \text{cm}$  radially away from the wafer flat (region B in Fig. 8a) was scanned. The imaged area,  $400 \times 200\ \mu\text{m}^2$  across the wide scribeline, was scanned as delineated at  $1\ \text{kHz}$  with a  $20\ \mu\text{m}$  step. Following preliminary exploratory scans, the purpose of this scan was to investigate the apparent effects on the PTR signal of the proximity of poly-Si pads to probed oxide layers. Therefore, the scanned area was confined within the delineated perimeter. It included the two parallel poly-Si rim lines on both sides of the scribeline, and the oxidized areas outside the scribeline. The amplitude image (Fig. 9a) of this area exhibits deep grooves (representing the straight parallel poly-Si rims of the scribeline) on both sides of the central line, which represents the signal from inside the scribeline. The back portion of the image borders the region close to the crossing point of this scribeline with the perpendicular scribeline. The signal strength decreases and the phase lag increases in the vicinity of the two frontal poly-Si pads, Fig. 9a and b. Both in the scribeline rim regions and in the area adjacent to poly-Si pads, it is speculated that this phenomenon may be due to enhanced recombination following photo-excited carrier diffusion in the neighborhood of heavily doped silicon, as the laser beam approaches the borders of the two pads within an ac electronic diffusion length  $L(\omega) = (D\tau)^{1/2}/(1 + i\omega\tau)$  [23]. This behavior is due to the fact that very high doping density strongly enhances the non-radiative (thermal) de-excitation probability of photo-excited carriers through collisional

events. As a result, the free-carrier-plasma density decreases dramatically due to thermal energy conversion, and so does the carrier-density-dominated PTR amplitude. This PTR signal change from electronic to thermal further shifts the phase centroid deeper into the bulk of the wafer through conduction heat transfer, thus increasing the PTR phase lag in those regions. Of further interest in this PTR scan is that both amplitude and phase images *inside the scribeline* show the same trends as those scanned on the oxide *outside the scribeline*, even though the scribeline is not in the immediate vicinity of the pads. Further line scans inside and alongside the entire length of this scribeline showed that the ac diffusion length is approx. 100  $\mu\text{m}$  in this region. This is on the order of the distance of the pads from the adjacent scribeline regions and corroborates the possibility of the influence of the pad structure on the recombination rate of diffusing photo-excited carriers.

#### 4. Conclusions

In this paper, I have described the physical and mathematical foundations of laser IR PTR as a promising NDT instrumentation technique currently being developed for emerging diffusion-wave materials depth profilometry and electronic quality-control metrologic technologies. Several case studies involving engineering steels, thermal-barrier coatings and semiconductor Si wafers have been presented. The remote, non-contact nature of this technique is rapidly finding applications in many industrial settings for ex situ characterization. Future developments in PTR hardware implementation are envisaged toward in situ use in the production line. Improvements in depth profilometry are anticipated in the speed and fidelity of thermal-diffusivity reconstructions, as well as in surface roughness modeling. Semiconductor lifetime and surface recombination velocity measurements using PTR provide the most convenient and non-intrusive method available to date. PTR has been shown to be capable of probing scribeline regions and, through those, the integrity of the in-line process, such as furnace contamination, substrate thermal cycling fatigue, dislocation propagation, defect creation, etc. The technology is expected to advance toward parallel signal processing and near-real-time wafer-surface lifetime mapping by use of fast ( $>1$  kHz) CCD imagers.

#### Acknowledgements

The support of Materials and Manufacturing Ontario (MMO) and the Natural Sciences and Engineering Research Council of Canada (NSERC) is gratefully acknowledged for most aspects of the development of both PTR technologies presented in this paper. The contributions of Jose Garcia, Mahendra Munidasa, Lena Nicolaidis and Mario Rodriguez to the case studies presented in this article are gratefully acknowledged.

#### References

- [1] Mandelis A. Diffusion waves and their uses. *Phys Today* 2000; 53(8–1):29–34.
- [2] Busse G, Walther HG. Photothermal nondestructive evaluation of materials with thermal waves. In: Mandelis A, editor. *Progress in photothermal and photoacoustic science and technology*, vol. 1. New York: Elsevier, 1992. p. 205–98.
- [3] French PC, Bond LJ. Finite-element modeling of Eddy-current nondestructive evaluation (NDE). *J Nondestruct Eval* 1988;7:55–70.
- [4] Mandelis A, editor. *Progress in photothermal and photoacoustic science and technology*, vol. 1. New York: Elsevier, 1992.
- [5] Mandelis A. Theory of photothermal wave diffraction tomography via spatial Laplace spectral decomposition. *J Phys A: Math Gen* 1991;24:2485–505.
- [6] Mandelis A, Peralta SB, Thoen J. Photoacoustic frequency-domain depth profiling of continuously inhomogeneous condensed phases. Theory and simulations of the inverse problem. *J Appl Phys* 1991;70:1761–70.
- [7] Munidasa M, Ma T-C, Mandelis A, Brown SK, Mannik L. Non-destructive depth profiling of laser processed Zr–2.5Nb alloy by infrared photothermal radiometry. *J Mater Sci Engng A* 1992;159: 111–8.
- [8] Fizez J, Thoen J. Thermal waves in materials with linearly inhomogeneous thermal conductivity. *J Appl Phys* 1994;75:7696–9.
- [9] Mandelis A, Funak F, Munidasa M. Generalized methodology for thermal diffusivity depth profile reconstruction in semi-infinite and finitely thick homogeneous solids. *J Appl Phys* 1996;80:5570–8.
- [10] Mandelis A, Schoubs E, Peralta SB, Thoen J. Photoacoustic depth profilometry of magnetic-field induced thermal diffusivity inhomogeneity in the liquid crystal octylcyanobiphenyl (8CB). *J Appl Phys* 1991;70:1771–7.
- [11] Lan TTN, Seidel U, Walther HG, Goch G, Schmitz B. Experimental results of photothermal microstructural depth profiling. *J Appl Phys* 1995;78:4108–11.
- [12] Mandelis A. Laser infrared photothermal radiometry of semiconductors: principles and applications to solid-state electronics. *Solid-State Electron* 1998;42:1–15.
- [13] Salnick A, Mandelis A, Ruda H, Jean C. Relative sensitivity of photo-modulated reflectance and photothermal infrared radiometry to thermal and carrier plasma waves in semiconductors. *J Appl Phys* 1997;82:1853–9.
- [14] Munidasa M, Funak F, Mandelis A. Application of a generalized methodology for quantitative thermal diffusivity depth profile reconstruction in manufactured inhomogeneous steel-based materials. *J Appl Phys* 1998;83:3498–595.
- [15] Leung WP, Tam AC. Techniques of flash radiometry. *J Appl Phys* 1984;56:153–61.
- [16] Press WH, Teukolsky SA, Vetterling WT, Flannery BP. *Numerical recipes in C*. 2nd ed. Cambridge, UK: Cambridge University Press, 1992. p. 203.
- [17] Munidasa M, Funak F, Mandelis A. Application of a generalized methodology for quantitative thermal diffusivity depth profile reconstruction in manufactured inhomogeneous steel-based materials. *J Appl Phys* 1998;83:3495–8.
- [18] Garcia J, Mandelis A, Farahbakhsh B, Lebowitz C, Harris I. Thermo-physical properties of thermal sprayed coatings on carbon steel substrates by photothermal radiometry. *Int J Thermophys* 1999;20:1587–602.
- [19] Salnick A, Jean C, Mandelis A. Noncontacting photothermal radiometry of SiO<sub>2</sub>/Si MOS capacitor structures. *Solid-State Electron* 1997;41:591–7.
- [20] Shockley W, Read WT. Statistics of the recombination of holes and electrons. *Phys Rev* 1952;87:835–42.
- [21] Hall RN. Electron-hole recombination in germanium. *Phys Rev* 1952;87:387.

- [22] Rodriguez ME, Mandelis A, Pan G, Nicolaides L, Garcia JA, Riopel Y. Computational aspects of laser radiometric multiparameter fit for carrier transport property measurements in Si wafers. *J Electrochem Soc* 2000;147:687–98.
- [23] Ikari T, Salnick A, Mandelis A. Theoretical and experimental aspects of three-dimensional infrared photothermal radiometry of semiconductors. *J Appl Phys* 1999;85:7392–7.
- [24] Mandelis A, Budiman RA, Vargas M, Wolff D. Noncontact photothermal infrared radiometric deep-level transient spectroscopy of GaAs wafers. *Appl Phys Lett* 1995;67:1582–4.